Research in Astron. Astrophys. **2012** Vol. **12** No. **12**, 1681–1692
http://www.raa-journal.org *http://www.iop.org/journals/raa*

***R**esearch in*
***A**stronomy and*
***A**strophysics*

Statistical study of emerging flux regions and the response of the upper atmosphere *

Jie Zhao and Hui Li

Purple Mountain Observatory, Chinese Academy of Sciences, Nanjing 210008, China;
nj.lihui@pmo.ac.cn
Key Laboratory of Dark Matter and Space Astronomy, Chinese Academy of Sciences, Nanjing 210008, China

Received 2012 April 26; accepted 2012 June 19

Abstract We statistically study the properties of emerging flux regions (EFRs) and response of the upper solar atmosphere to the flux emergence using data from the Helioseismic and Magnetic Imager and the Atmospheric Imaging Assembly onboard the Solar Dynamics Observatory. Parameters including total emerged flux, flux growth rate, maximum area, duration of the emergence and separation speed of the opposite polarities are adopted to delineate the properties of EFRs. The response of the upper atmosphere is addressed by the response of the atmosphere at different wavelengths (and thus at different temperatures). According to our results, the total emerged fluxes are in the range of (0.44–11.2)$\times 10^{19}$ Mx while the maximum area ranges from 17 to 182 arcsec^2. The durations of the emergence are between 1 and 12 h, which are positively correlated to both the total emerged flux and the maximum area. The maximum distances between the opposite polarities are 7–25 arcsec and are also positively correlated to the duration. The separation speeds are from 0.05 to 1.08 km s^{-1}, negatively correlated to the duration. The derived flux growth rates are (0.1–1.3)$\times 10^{19}$ Mx h^{-1}, which are positively correlated to the total emerging flux. The upper atmosphere first responds to the flux emergence in the 1600Å chromospheric line, and then tens to hundreds of seconds later, in coronal lines, such as the 171Å ($T = 10^{5.8}$ K) and 211Å ($T = 10^{6.3}$ K) lines almost simultaneously, suggesting the successive heating of the atmosphere from the chromosphere to the corona.

Key words: Sun: magnetic fields — Sun: UV radiation — Sun: corona

1 INTRODUCTION

The ubiquitous emerging flux regions (EFRs) on the Sun with a variety of sizes, lifetimes, total magnetic fluxes and field strengths have been widely discussed. Magnetic features can cover a large scale, such as sunspots that have fluxes of about 10^{22} Mx (Maxwell), and generally exist in active regions (Thornton & Parnell 2011). Magnetic features with a small scale such as network fields and intranetwork (IN) fields have fluxes of 10^{18}–10^{19} Mx (Martin 1988; Wang et al. 1995) and 10^{16}–10^{18} Mx (Livingston & Harvey 1975; Martin et al. 1985; Zirin 1987; Keller et al. 1994; Wang et al.

* Supported by the National Natural Science Foundation of China.

1995) respectively and generally exist in the quiet Sun. Using data from the high-resolution *Hinode* (Kosugi et al. 2007) Solar Optical Telescope (SOT, Tsuneta et al. 2008), Thornton & Parnell (2011) developed two different feature identification methods to determine the rate of flux emergence for small-scale magnetic features in the quiet Sun. Combined with previous results, they found that the frequency of emergence followed a power-law distribution with fluxes which ranged from 10^{16} to 10^{23} Mx. Simon et al. (2001) investigated dipoles in the photosphere from emerging to splitting and then ending up in the magnetic network. They assumed a flux emergence rate of 7×10^{22} Mx d^{-1} (consistent with what was indicated by others for ephemeral regions (ERs)) that could keep the solar surface at a steady state. Hagenaar (2001) also examined a large number of ERs and obtained the total amount of flux emergence to be 5×10^{23} Mx d^{-1}. He concluded that the magnetic field in the quiet Sun could be replaced in 14 h with this rate of emergence. When EFRs go through the atmosphere of the Sun, they produce various solar activities including Ellerman bombs, blinkers, small scale transient brightenings and solar flares, filament eruptions and large scale coronal mass ejections (CMEs) as viewed by Low (1996) and heat the upper atmosphere (Li et al. 2007; Li & Li 2010).

When a new EFR appears, it may interact with the pre-existing surrounding region and produce a tiny two-ribbon flare (Sakajiri et al. 2004) or an EFR-surge which is the first signature of magnetic flux emergence in many EFRs (Kurokawa & Kawai 1993). The evolution of two consequent dipoles in the coronal hole (CH) was first reported by Yang et al. (2009). The two dipoles interacted with each other and produced a jet and a plasma eruption. Their work is meaningful for the investigation of CH evolution. Using the multi-wavelength observations combined with a nonlinear force-free extrapolation, Valori et al. (2012) provided a coherent picture of the emergence process of small-scale magnetic dipoles, which subsequently reconnected to form a large scale structure in the corona. Granular-scale flux emergence, which led to cancelation at the penumbral boundary, was studied by Lim et al. (2011). They used data from the New Solar Telescope (NST, Goode et al. 2010) at Big Bear Solar Observatory (BBSO, Cao et al. 2010) with a high spatial and temporal resolution. A bright point (BP) that developed in their case was due to the cancelation. They thought that the scale of ER in their work was about 0.5–1 arcsec, which was not detected in a magnetogram obtained with the Helioseismic and Magnetic Imager (HMI, Schou et al. 2012).

Hagenaar et al. (2008) investigated the evolution of magnetic network elements in the photosphere of the quiet-Sun with data from the Michelson Doppler Imager (MDI, Scherrer et al. 1995) and found that the ER emergence rate is higher in flux-balanced regions.

Wang et al. (2012) studied the solar IN magnetic elements. They found the flux emergence in these regions was mainly in the form of cluster emergence of mixed polarities and IN ERs. The samples in their work have an average separation of 3–4 arcsec and a lifetime of 10–15 min, which are relatively small. Zhang et al. (2009) selected six events from the *Hinode* Spectro-Polarimeter (SP, Lites et al. 2001) data to investigate the interaction between granulation and small-scale magnetic flux. Their result implies that the granule evolves quite differently according to the topology and emergence location of the EFR. Meanwhile, the granular flow also influences the development of the EFR. With BBSO data, Zhang et al. (2006) compared the distribution of the magnetic flux in a CH and a quiet region (QR). Their result demonstrates a balanced flux distribution in the QR and an imbalanced distribution in the CH, for IN fields and network fields.

Yang et al. (2012) also statistically investigated the ERs in the quiet Sun and found two types of ERs: normal ERs and self-canceled ERs. Their results also reveal that the ERs with a higher magnetic flux tend to be more commonly self-canceling. A statistical study about EFRs has also been done with SOT onboard the *Hinode* satellite by Otsuji et al. (2007, 2011). In the first paper they found the two polarities separated from each other at a speed of 4.2 km s^{-1} during the initial phase and then the separation speed decreased to about 1 km s^{-1} ten minutes later. In the second paper, they demonstrated that the maximum spatial distance between the two main polarities, the magnetic flux growth rate and the mean separation speed, follow a power-law distribution with the

total emerged flux. More works about magnetic fields can also be found in the review of Fang (2011) and other references.

EFRs are probably the brightest features in the non-flaring solar corona (Schmieder et al. 2004). Responding to the flux emergence, the coronal loops may appear bright in all temperatures. The Yohkoh Soft X-ray Telescope (SXT, Tsuneta et al. 1991) has observed many transient brightenings (Shimizu et al. 1992, 1994) in coordinated multi-wavelength observations, which are located in EFRs. The close relationship between the emerging flux and transient brightenings has been extensively studied (Mein et al. 2001; Kubo et al. 2003). Zhang et al. (2012) carried out a detailed multi-wavelength analysis of two coronal bright points (CBPs) and proposed that the gentle brightenings and CBP flashes might be due to a null-point reconnection and the separatrix reconnection, respectively.

Even though the SOT has observed many EFRs and some statistical work has been done to study the EFR's properties (Otsuji et al. 2011), more work is still needed since the results are far from determined due to the wide span of their lifetimes, total fluxes, areas, etc. Meanwhile, due to the intimate association of EFRs with various solar activities, statistical study of the properties of EFRs and the resultant response of the upper atmosphere is important for understanding the physics of the solar active regions and activities.

In this paper, we use data from the HMI and the Atmospheric Imaging Assembly (AIA, Lemen et al. 2012) onboard the *Solar Dynamics Observatory* (*SDO*, Pesnell et al. 2012) to study the properties of EFRs and the corresponding response of the upper solar atmosphere. In Section 2, we introduce the observations and data reduction. We give one example to demonstrate a case study and the statistical results in Section 3. Our discussion and summary are presented in Section 4.

2 OBSERVATIONS AND DATA REDUCTION

We used the iSolSearch tool from the Heliophysics Events Knowledgebase (HEK) system (*http://www.lmsal.com/isolsearch*) to select EFRs for our study, which allowed us to easily find EFRs and download data for the required field-of-view (FOV) to save time and computer disk space. The studied EFRs were selected according to the following three criteria: (1) they appear close to the disk center to minimize the projection effect of the coronal observation, namely, the response in extreme ultraviolet (EUV) wavebands; (2) they are relatively simple and do not have an interaction with other EFRs to guarantee the accuracy of the computed separation and subsequently the separation speed (see definition below for these parameters); (3) they continue emerging for at least one hour. Based on these requirements, we selected 50 EFRs to conduct this study, which appeared during the times 2010 September 2–6, 2011 August 27–29, 2011 September 10 or 2011 October 21.

The HMI instrument on the *SDO* observes the full solar disk in the Fe I absorption line at 6173 Å with a resolution of 1 arcsec. It provides four main types of data: dopplergrams (maps of solar surface velocity), continuum filtergrams (broad-wavelength photographs of the solar photosphere), and both line-of-sight (LOS) and vector magnetograms (maps of the photospheric magnetic field). The AIA onboard the *SDO* obtains full disk images in multiple EUV and ultraviolet (UV) passbands with a resolution of 1.2 arcsec. The two instruments provide the first full-disk continuous observations of solar magnetic fields and the solar atmosphere, respectively. HMI obtains the LOS magnetic field with a 45 s cadence and AIA records coronal images with a 12 s cadence.

In our study, we adopt 12 min HMI LOS field data. Considering that the magnetic field evolves slowly with respect to the duration of the EFR, data with such a cadence are acceptable to describe the properties of the EFR. The downloaded HMI magnetic field data have been calibrated. We downloaded AIA images in a partial form based on the region that the EFR is in, such as 1600 Å, 304 Å, 171 Å, 193 Å, or 211 Å lines, which are formed at temperatures in the upper chromosphere and corona. The downloaded AIA images are prepared in a standard manner including bad-pixel removal, despiking and flat-fielding. Both HMI and AIA data are corrected for differential rotation.

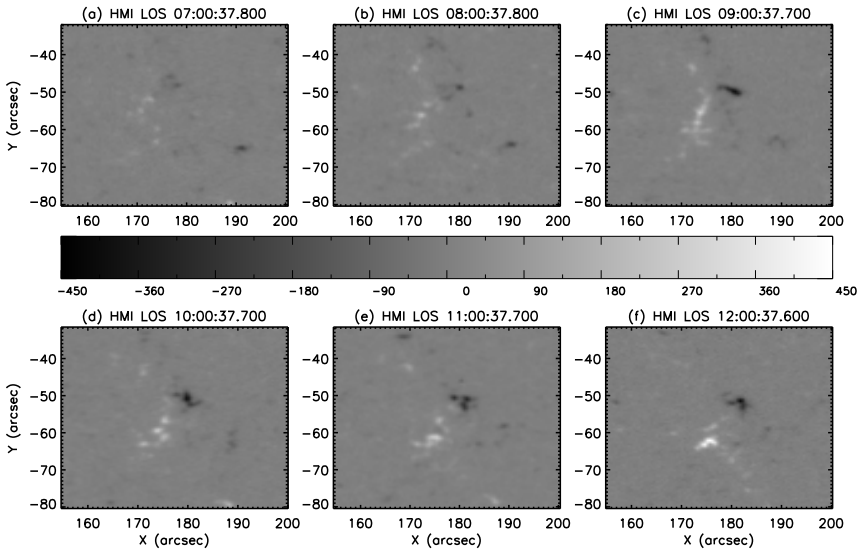

Fig. 1 LOS magnetograms obtained with *SDO*/HMI. This event lasted from 07:00 UT to 12:00 UT on 2010 September 5, which covers the time range of the studied EFR in the paper. The scale bar in the middle indicates the magnetic field strength in Gauss.

The HMI and AIA images are coaligned by coaligning the HMI intensity image and AIA white-light (WL) image.

To study the properties of EFRs, we derive the following parameters from the HMI LOS magnetic field data: (1) duration of emergence (time span from the start to the maximum flux), (2) total emerged flux (maximum flux subtracted by the flux before emergence), (3) flux growth rate (total emerged flux divided by the duration of emergence), (4) maximum area (the maximum value for the area of the EFR), (5) average field strength (arithmetic mean value of the field strength, which is calculated through the total emerged flux divided by the area), (6) separation (distance between the two opposite polarities), and (7) separation speed (fitting result from the time profile of the separation).

3 RESULTS

3.1 Example

We present the event that happened on 2010 September 5 as a case study. The evolution of this EFR is shown in Figure 1. This EFR appeared before 07:00 UT and we can see the two polarities (even though they are weak) located at the upper-left corner from the center in panel (a). In this rectangular region, a single negative pole exists at the lower-right corner and we can still see it in panel (b). However, this rectangular area is relatively clear from 09:00 UT since the EFR has developed and become the main feature in this region. The distance between opposite polarities obviously increased after 07:00 UT and changed slightly after 10:00 UT. The magnetic dipole seems to move slightly from the upper-left to the lower-right, which may suggest that the convective flow is coupling with the magnetic field during flux emergence.

Images from three of the five selected AIA channels are presented in Figure 2. The AIA/1600 Å, 171 Å, and 211 Å intensity maps are shown in the left column, middle column and right column, respectively. All of them are recorded from 07:00 UT to 11:00 UT. The region has the same FOV

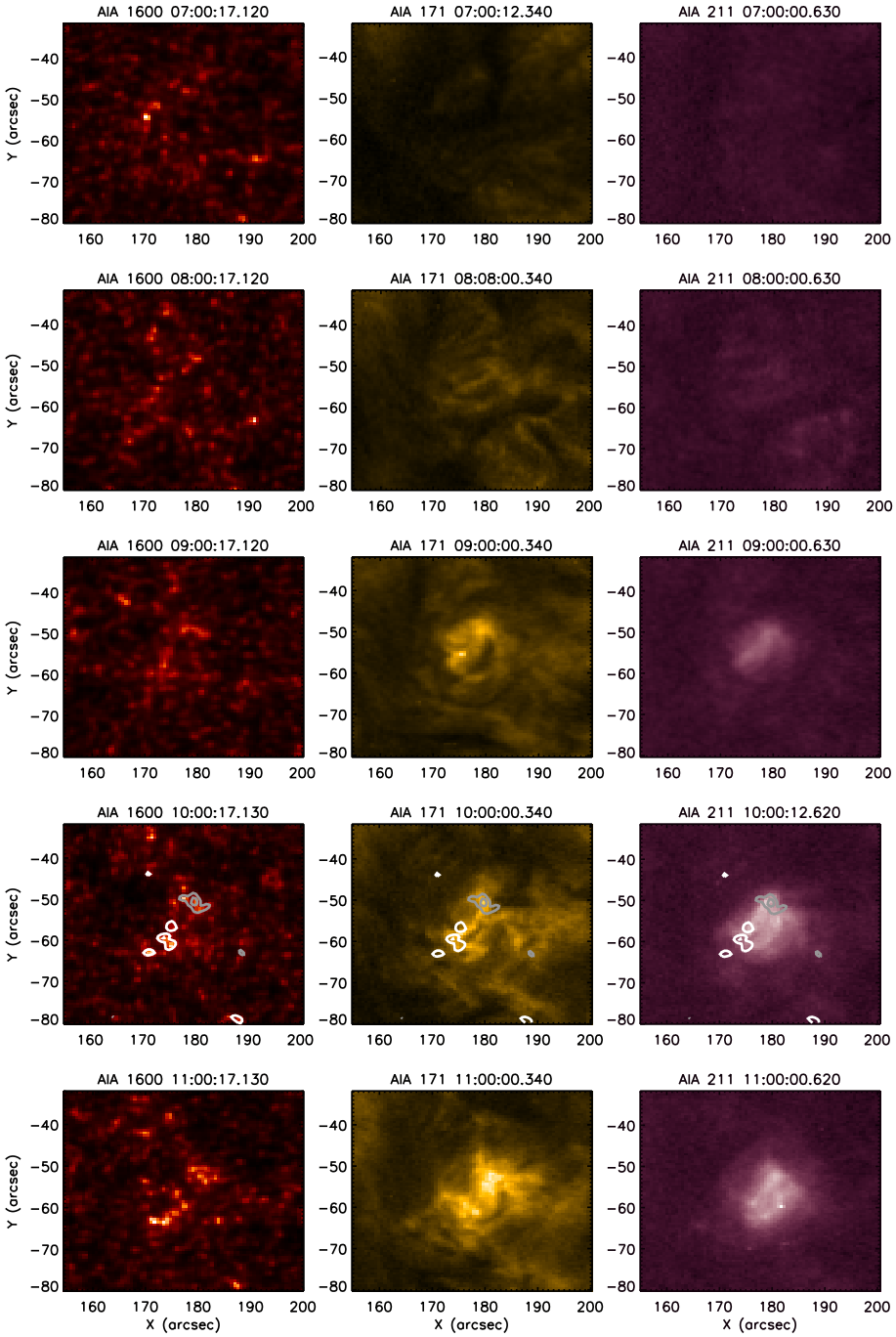

Fig. 2 Evolution of the response in the upper atmosphere from AIA/1600 Å (*left column*), 171 Å (*middle column*), and 211 Å (*right column*) lasts from 07:00 UT to 11:00 UT in the same region as in Figure 1. The contours overlaid on the 10:00 UT panels are the LOS magnetic field with a strength of 80, 250, −80, and –250 G. The white and gray lines correspond to positive and negative polarities, respectively.

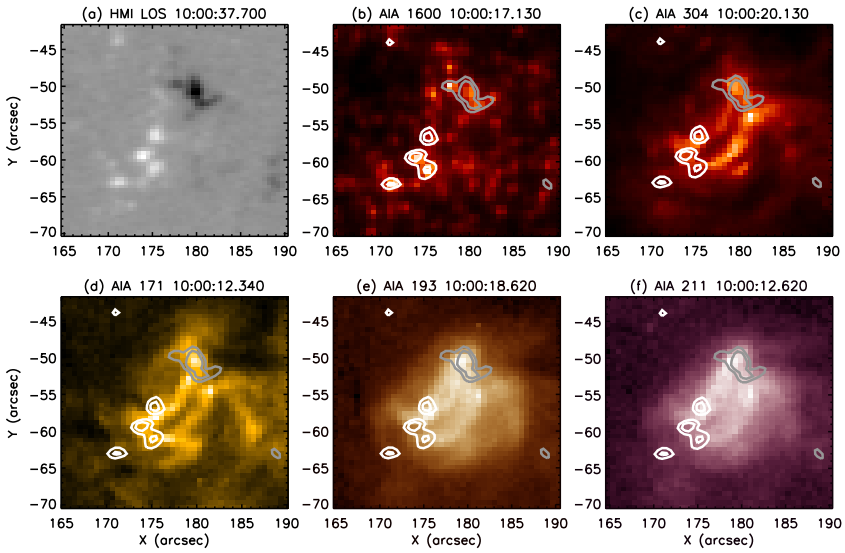

Fig. 3 LOS magnetogram and its corresponding AIA intensity maps in 1600 Å, 304 Å, 171 Å, 193 Å, and 211 Å. The region is a little smaller than the ones in Figs. 1 and 2. The contours overlaid on the intensity maps are the LOS magnetic field with a strength of 80, 160, –80, and –160 G. The white and gray lines correspond to the positive and negative polarities, respectively.

as the rectangular area in Figure 1 and three intensity maps at 10:00 UT are overlaid with contours of the magnetic field at the same time. The contours manifest that the magnetic dipole corresponds to the chromospheric brightening features and footpoints of the coronal loops. In 171 Å and 211 Å intensity maps, coronal loops become larger and brighter with time although we can just see two obvious brightening features in the 1600 Å intensity maps.

We show the LOS magnetogram together with five intensity maps of AIA in Figure 3 with the same area in which we calculate the parameters mentioned in Section 2. The contours overlaid on the intensity maps correspond to the magnetic dipole.

The area that we select to calculate the parameters mentioned above is of a proper size in order not to include other magnetic structures as shown in Figure 1(a). We use ± 20 G as the background magnetic field when computing the magnetic flux of the EFR, which is shown in Figure 4(a). It clearly manifests an emerging event in this region, which started before 06:00 UT and reached its maximum at about 10:00 UT as indicated by the vertical lines. The start time of emergence is defined to be the time when the magnetic flux continuously increases while the end time of emergence is chosen to be the time when the magnetic flux reaches its maximum. The span of these two times is defined as the duration of the EFR. The area of the EFR is obtained by summing all pixels with a magnetic field strength larger than 20 G or less than –20 G. With this threshold, we determine the average magnetic field strength in the EFR (Fig. 4(b)). It only gives the area and average magnetic field of the negative pole of the EFR. We should mention that even though we tried to choose a region that only contained the EFR that we are interested in, the region may have other magnetic features that subsequently affect the result, such as the magnetic flux of the EFR. Hence, we will pick the polarity with a smaller maximum magnetic flux to represent the whole EFR. In this example, the maximum magnetic flux with negative polarity is smaller, so it is more suitable to represent the EFR.

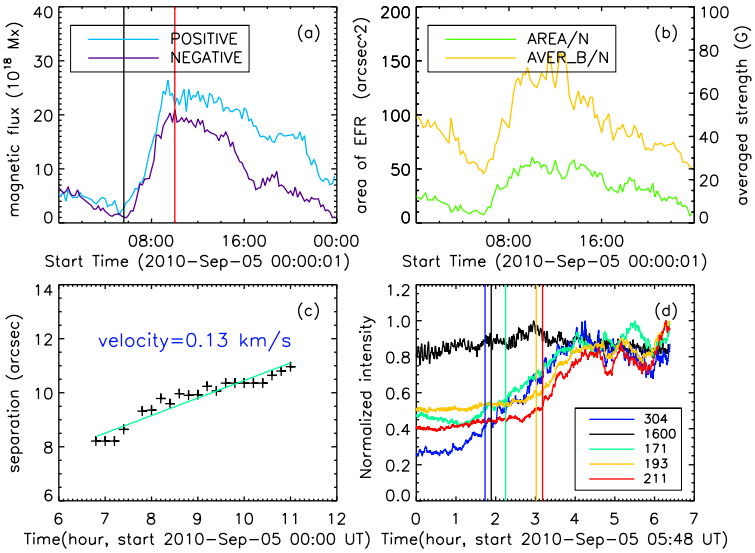

Fig. 4 Panel (a) shows the evolution of magnetic flux in the region which is presented in Fig. 3(a). The vertical lines indicate the start and end time of the emergence, respectively. Panel (b) gives variations in the area and average magnetic field strength of the EFR in the same region as panel (a). Evolution of distance between the opposite polarities of the EFR is shown in panel (c). The green line indicates the fitting result. We exhibit light curves of the 5 AIA channels in panel (d) which all start from 05:48 UT on 2010 September 5. The vertical lines indicate the start times of the response in the same colors.

Using an IDL program ('label-region.pro'), we can label the connected domain in this rectangular area, then the distance between the two polarities is calculated and shown in Figure 4(c). We show the variation in distance after 06:00 UT, but keep in mind that the EFR appeared before 06:00 UT although it is faint in the magnetogram. Since the EFR is very small and faint in the magnetogram at the beginning, our method may capture other features, which are more obvious at that time. When the EFR becomes the main features in the region, at that point we need the derived distance. Consequently we ignore the initial phase when computing the separation speed if there are other features. The separation speed is easy to obtain by fitting the evolution curve of distance between the two polarities. For this EFR, a velocity of 0.13 km s^{-1} is obtained.

From the *SDO*/AIA data, we obtained light-curves of the five layers from the chromosphere to the corona, which are shown in Figure 4(d). The curves all start from 05:48 UT on 2010 September 5 when the emergence started. All of them continuously increase after the EFR appears and the light curves with a higher temperature seem to start increasing later. The background values of the five channels are the average intensities from 05:48 UT to 06:30 UT. When the value reaches 20% of the maximum increment, we define this time as the response time of the atmosphere.

3.2 Statistical Results

There are 50 EFRs selected for our study in this paper. We downloaded all the corresponding AIA data for the 50 events and found only half of them can give us a relatively accurate start time of the response, but the others show fluctuating light curves that cannot be used to determine the start time.

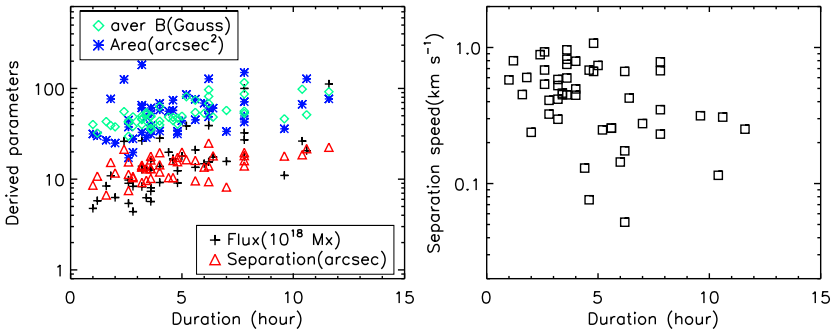

Fig. 5 Distributions of the derived emerged flux, maximum area, separation and average field strength (*left*) and separation speed (*right*) with the duration of emergence for the studied EFRs.

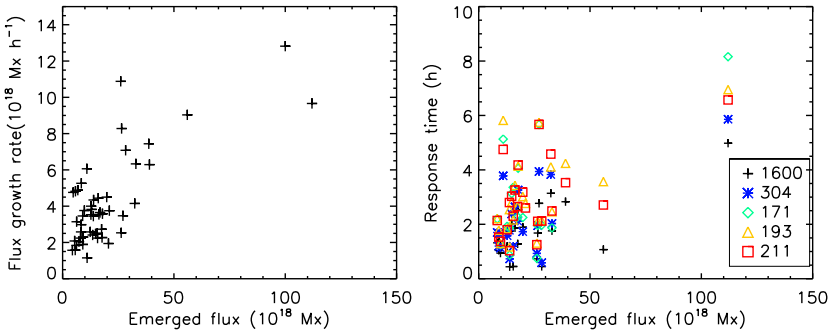

Fig. 6 Distributions of flux growth rate (*left*) and response time of different AIA wavelengths with respect to the start time of flux emergence (*right*).

Table 1 gives a list of the selected EFRs and their basic information. All events are listed according to the order of increment for magnetic flux. The polarity in Table 1 means the polarity of the EFR, which we used to compute the parameters. Other parameters listed in the table have all been mentioned above. There are two events (20110827D and 20111021D) for which we cannot obtain the separation and separation speed.

In the 50 events, 17 have fluxes less than 10^{19} Mx, 31 have fluxes in the range of (10^{19}–10^{20}) Mx and only 2 have fluxes more than 10^{20} Mx. According to the results, the emerged fluxes are in the range (0.44–11.2)$\times10^{19}$ Mx while the derived flux growth rates are (0.1–1.3)$\times10^{19}$ Mx h^{-1}. The maximum area ranges from 17 to 182 arcsec^2 and the average magnetic field strength is 29.7–116.1 G. The durations of the emergences are between 1 and 12 h. The maximum distances between the opposite polarities are 7–25 arcsec while the separation speeds are from 0.05 to 1.08 km s^{-1}.

To check the relationship among the parameters, which describes the property of EFRs, we make the scatter plots in Figure 5 and the left panel of Figure 6. The result shows that the emerged flux, area, average magnetic field strength and separation are all positively correlated to the duration of emergence, but the separation speed is negatively correlated to the duration of emergence. The rate of emergence is positively correlated to the emerged flux.

Table 1 Basic Information and Derived Parameters for the Studied EFRs

EFR number	Polarity	Flux (10^{19} Mx)	Duration (h)	Emergence rate (10^{18} Mx h^{-1})	Area (arcsec^2)	Aver B (G)	Separation (arcsec)	Sep speed (km s^{-1})
20110827C	+	0.44	2.8	1.57	19.7	38.2	10.7	0.41
20100902E	–	0.48	1.0	4.76	31.5	40.1	8.6	0.58
20100905C	–	0.54	2.6	2.08	17.2	29.7	7.5	0.54
20100902F	–	0.57	3.6	1.58	35.5	36.5	17.9	0.96
20110827A	+	0.58	1.2	4.82	30.0	32.3	10.8	0.8
20100902D	–	0.62	3.4	1.84	28.7	54.4	9.7	0.46
20110827E	–	0.63	2.0	3.14	25.0	37.8	11.7	0.24
20110827D	–	0.68	1.4	4.88	26.4	30.6	–	–
20100902B	+	0.74	3.6	2.04	31.4	35.2	10.2	0.75
20100902G	–	0.81	3.6	2.24	38.8	49.9	13.1	0.6
20110827G	–	0.83	3.2	2.58	32.8	39.9	9.2	0.42
20100903F	–	0.83	2.8	2.98	27.8	48.7	10.4	0.32
20100902C	–	0.84	1.6	5.26	26.9	43.2	6.7	0.45
20111021E	–	0.90	2.6	3.46	30.7	42.6	11.3	0.93
20110827B	+	0.91	4.8	1.89	33.7	40.4	15.6	0.67
20100906C	–	0.92	4.0	2.3	33.9	43.7	19.6	0.79
20100903D	+	0.98	2.6	3.76	37.6	43.2	15.5	0.68
20110829A	+	1.1	1.8	6.06	76.7	39.1	15.3	0.6
20100905A	–	1.1	9.6	1.15	35.9	46.3	18	0.32
20100905F	–	1.24	4.8	2.58	31.5	47.2	17.4	1.08
20100903E	–	1.27	3.6	3.53	52.9	48.9	13.1	0.45
20110910E	+	1.28	3.2	4.0	42.7	45.4	13.6	0.58
20100903B	–	1.3	3.4	3.82	48.4	51.7	13	0.45
20110827I	+	1.35	5.6	2.41	45.1	54.5	9.6	0.26
20100902H	+	1.38	4.0	3.45	58	39.7	12	0.45
20110910D	–	1.39	3.2	4.34	76.1	46.3	13.8	0.3
20110828B	–	1.48	6.0	2.47	69	53.2	13.6	0.14
20100903C	–	1.55	6.2	2.5	48.8	68.3	9.4	0.05
20110827J	+	1.57	7.0	2.24	33.6	57.3	8.2	0.28
20110829B	+	1.6	3.6	4.44	60.9	40	16.3	0.82
20100906D	–	1.63	4.6	3.54	57.3	44.3	16.1	0.68
20110827F	+	1.68	4.6	3.65	74.2	48.1	10.4	0.08
20100903A	–	1.75	6.4	2.73	60.6	48.4	18.1	0.43
20110828A	+	1.77	7.8	2.27	71.4	53.1	19.7	0.79
20100905B	+	1.79	5.0	3.58	44.1	49.5	19.9	0.74
20100905D	–	1.98	4.4	4.5	56.1	48.4	10.4	0.13
20110829C	–	2.06	10.6	1.94	66.8	51.3	21.7	0.31
20111021B	+	2.1	5.6	3.75	44.8	74.4	16.1	0.26
20100906A	+	2.61	2.4	10.88	125.7	55.6	21.4	0.89
20110910C	+	2.63	10.4	2.53	149.9	98.2	18.6	0.11
20100902A	+	2.65	3.2	8.28	65.3	49.7	14.3	0.52
20100905E	+	2.71	7.8	3.47	49.8	56.2	14	0.23
20100906B	–	2.83	4	7.08	68.4	63.2	14.4	0.5
20111021C	+	3.24	7.8	4.15	80.3	86.9	16.0	0.68
20111021D	–	3.29	5.2	6.33	87.1	56.9	–	–
20110827H	–	3.87	5.2	7.44	85.9	81.2	16.4	0.25
20110828C	+	3.9	6.2	6.29	127.7	81.8	25	0.68
20110910B	–	5.6	6.2	9.03	61.2	96.8	14	0.17
20111021A	+	10	7.8	12.8	111.4	116.1	18.2	0.35
20110910A	–	11.2	11.6	9.66	182.2	92	22.5	0.25

After preparing the downloaded AIA images, we calculate the brightness of each EFR in five wavebands, i.e., 1600 Å, 304 Å, 171 Å, 193 Å and 211 Å, and subsequently derive the corresponding light-curves in order to study the response of the upper solar atmosphere to the relevant flux emergence. We define the start of the UV/EUV brightening to be when the brightness has increased by

Table 2 Time Delay of the Five Selected AIA Channels with Respect to the Start Time of Flux Emergence

EFR	Flux	Time delay (h)				
number	(10^{19} Mx)	1600	304	171	193	211
20100903F	0.83	1.3	1.7	2.2	2.2	2.1
20111021E	0.90	1.0	1.2	–	1.8	1.5
20110827B	0.91	1.1	1.9	1.1	–	–
20100906C	0.92	1.3	1.7	–	–	–
20100903D	0.98	0.9	1.1	1.3	1.3	1.4
20100905A	1.1	–	3.8	5.1	5.8	4.8
20110910E	1.28	1.2	1.6	1.9	1.8	1.8
20100902H	1.38	1.8	1.8	1.9	2.5	2.8
20110910D	1.39	0.4	0.7	0.9	1.2	1.0
20110828B	1.48	2.0	2.4	3.1	2.8	3.0
20100903C	1.55	0.5	1.2	3.4	2.2	2.3
20100906D	1.63	1.9	2.6		3.4	3.3
20100903A	1.75	1.3	2.1	2.3	2.7	2.7
20110828A	1.77	2.5	3.3	4.1	4.1	4.2
20100905D	1.98	1.9	1.7	2.2	3.0	3.2
20111021B	2.1	–	–	–	2.8	2.6
20100906A	2.61	0.7	0.9	0.7	1.3	1.2
20100902A	2.65	1.7	2.0	2.0	2.1	2.1
20100905E	2.71	2.8	3.9	5.7	5.7	5.7
20100906B	2.83	0.4	0.6	2.0	2.1	2.1
20111021C	3.24	3.1	3.8	–	4.1	4.6
20111021D	3.29	1.8	2.0	1.9	2.5	2.5
20110828C	3.9	2.8	–	–	4.2	3.5
20110910B	5.6	1.1	–	–	3.6	2.7
20110910A	11.2	5.0	5.9	8.2	6.9	6.6

20% of the maximum enhancement and then compute the time delay of the UV/EUV brightening with respect to the start of flux emergence.

Table 2 gives a list of EFRs with the corresponding response in the upper atmosphere, of which, the upper part (twenty percent) has fluxes less than 10^{19} Mx while the remaining lower part has fluxes of more than 10^{19} Mx. The response times of the five channels are all calculated according to the start of flux emergence. In this way, we get response times in the range of (0.4–5.0), (0.6–5.9), (0.7–8.2), (1.2–6.9) and (1.2–6.6) h in 1600 Å, 304 Å, 171 Å, 193 Å and 211 Å, respectively.

The results are also displayed in Figure 6 (right panel). It is shown that the upper atmosphere first responds to the flux emergence in the 1600 Å chromospheric line in half an hour to about 5 hours, and then tens to hundreds of seconds later, it responds in coronal lines, such as the 171 Å ($T = 10^{5.8}$ K) and 211 Å ($T = 10^{6.3}$ K) lines.

4 DISCUSSION AND CONCLUSIONS

Using the LOS magnetic field data from the *SDO*/HMI, we statistically studied the properties of EFRs through the seven parameters mentioned above. The inferred relationship of these parameters is generally consistent with previous results (e.g. Otsuji et al. 2007, 2011). We found that the durations have a larger range (1–12 h) in our case. All the parameters show a weak positive correlation with total emerged flux except for the separation speed, which decreases as the emerged flux increases. This is consistent with the conclusion that tubes of larger EFRs are anchored in deeper layers (Javaraiah & Gokhale 1997).

Meanwhile, for EFRs with flux less than 10^{19} Mx, in our cases the upper atmosphere does not show apparent brightness enhancement in coronal lines, indicating that small EFRs tend to interact with a low-layer magnetic structure. However, the heating effect by ERFs on the lower atmosphere with a flux less than 10^{19} Mx is not persistent but rather fluctuates. We deduce that in the lower atmosphere, the magnetic structures tend to be smaller and lower; when small EFRs that are comparable with the surrounding magnetic structures appear, the interaction between them will greatly change the morphologies of both. This will not guarantee continuous heating.

But when the EFR is larger (here we say with a flux greater than 10^{19} Mx), the interaction between the EFR itself and the surrounding magnetic structures may not dramatically change the morphology of the EFR and when it emerges into the corona where the surrounding magnetic structures are larger and higher, the surrounding magnetic structures may ensure the successive heating. All of these suppositions need simulations to confirm the associated theories.

In previous papers of Otsuji et al. (2007, 2011), they used data from the *Hinode*/SOT which only observes a partial area of the sun during a certain time frame. Therefore they might not have considered as many parameters as we have, since the data obtained by the SOT probably do not cover the whole duration of the event, e.g. it misses the beginning phase or it did not contain the phase when magnetic flux reached the maximum. However, we can get the entire information about an EFR as long as we download abundant data thanks to the continuous observations of the *SDO*. Therefore, our statistical result may be more reliable since we have data covering the entire process of the emergence.

The statistical research for the response of the upper atmosphere has already been studied by Li et al. (2007) and Li & Li (2010), and their works either did not have magnetic information (Li & Li 2010) or the time resolution was too low (Li et al. 2007). In this paper, we have both the LOS magnetogram and five channels of UV/EUV observations for the chromosphere and corona with a time resolution of 12 seconds. The result shown in Figure 6 (right panel) manifests that the emerging flux should first reach and heat the chromosphere, and then move to the corona and cause the coronal brightening. It is also mentioned in Li et al. (2007) that one could expect that the chromosphere displays enhanced brightening in the Ca II H line earlier than the corona in soft X-rays, but later than the increase of the integrated magnetic flux. It also manifests that the response time delay is much longer for a larger emerged flux. A larger EFR interacts with its surroundings for a longer time and subsequently the heating process lasts longer.

It should be mentioned that in our study, we use HMI LOS magnetic field data with a 12 min cadence, which is relatively small compared with the duration of the EFRs and certainly has some effect on our results, which may induce an uncertainty of 12 min for the time delay between flux emergence and upper response. However, it is still relatively small when compared with the response time in this paper. The threshold (20% of the maximum enhancement) used to define the start time of the EUV response could also slightly affect the time delay. However, these do not change our results as a whole.

In summary, from this statistical study we found that the derived parameters for EFRs generally have a large range, and all the durations, areas, separations, flux growth rates and average field strength have a weak positive correlation with the total emerged flux. EUV emissions are also related to the total emerged flux and are delayed with respect to the flux emergence by minutes to hours. The chromosphere responds to flux emergence first and then the corona. The delay time increases with the temperature of the EUV emission, suggesting the successive heating of the upper atmosphere.

Acknowledgements This work was supported by the National Natural Science Foundation of China (Grant Nos. 10873038 and 10833007) and the National Basic Research Program of China (973 Program, 2011CB811402). The authors are grateful to the NASA/*SDO*, AIA and HMI science teams for the data.

References

Cao, W., Gorceix, N., Coulter, R., et al. 2010, Astronomische Nachrichten, 331, 636
Fang, C. 2011, RAA (Research in Astronomy and Astrophysics), 11, 1377
Goode, P. R., Coulter, R., Gorceix, N., Yurchyshyn, V., & Cao, W. 2010, Astronomische Nachrichten, 331, 620
Hagenaar, H. J. 2001, ApJ, 555, 448
Hagenaar, H. J., De Rosa, M. L., & Schrijver, C. J. 2008, ApJ, 678, 541
Javaraiah, J., & Gokhale, M. H. 1997, A&A, 327, 795
Keller, C. U., Deubner, F.-L., Egger, U., Fleck, B., & Povel, H. P. 1994, A&A, 286, 626
Kosugi, T., Matsuzaki, K., Sakao, T., et al. 2007, Solar Phys., 243, 3
Kubo, M., Shimizu, T., & Lites, B. W. 2003, ApJ, 595, 465
Kurokawa, H., & Kawai, G. 1993, in IAU Colloq. 141, The Magnetic and Velocity Fields of Solar Active Regions, Astronomical Society of the Pacific Conference Series, 46, eds. H. Zirin, G. Ai, & H. Wang, 507
Lemen, J. R., Title, A. M., Akin, D. J., et al. 2012, Solar Phys., 275, 17
Li, H., Sakurai, T., Ichimito, K., et al. 2007, PASJ, 59, 643
Li, J.-W., & Li, H. 2010, RAA (Research in Astronomy and Astrophysics), 10, 696
Lim, E.-K., Yurchyshyn, V., Abramenko, V., et al. 2011, ApJ, 740, 82
Lites, B. W., Elmore, D. F., & Streander, K. V. 2001, in Astronomical Society of the Pacific Conference Series, 236, Advanced Solar Polarimetry – Theory, Observation, and Instrumentation, ed. M. Sigwarth, 33
Livingston, W. C., & Harvey, J. 1975, in Bulletin of the American Astronomical Society, 7, 346
Low, B. C. 1996, Solar Phys., 167, 217
Martin, S. F. 1988, Solar Phys., 117, 243
Martin, S. F., Livi, S. H. B., & Wang, J. 1985, Australian Journal of Physics, 38, 929
Mein, N., Schmieder, B., DeLuca, E. E., et al. 2001, ApJ, 556, 438
Otsuji, K., Shibata, K., Kitai, R., et al. 2007, PASJ, 59, 649
Otsuji, K., Kitai, R., Ichimoto, K., & Shibata, K. 2011, PASJ, 63, 1047
Pesnell, W. D., Thompson, B. J., & Chamberlin, P. C. 2012, Solar Phys., 275, 3
Sakajiri, T., Brooks, D. H., Yamamoto, T., et al. 2004, ApJ, 616, 578
Scherrer, P. H., Bogart, R. S., Bush, R. I., et al. 1995, Solar Phys., 162, 129
Schmieder, B., Rust, D. M., Georgoulis, M. K., Démoulin, P., & Bernasconi, P. N. 2004, ApJ, 601, 530
Schou, J., Scherrer, P. H., Bush, R. I., et al. 2012, Solar Phys., 275, 229
Shimizu, T., Tsuneta, S., Acton, L. W., Lemen, J. R., & Uchida, Y. 1992, PASJ, 44, L147
Shimizu, T., Tsuneta, S., Acton, L. W., et al. 1994, ApJ, 422, 906
Simon, G. W., Title, A. M., & Weiss, N. O. 2001, ApJ, 561, 427
Thornton, L. M., & Parnell, C. E. 2011, Solar Phys., 269, 13
Tsuneta, S., Acton, L., Bruner, M., et al. 1991, Solar Phys., 136, 37
Tsuneta, S., Ichimoto, K., Katsukawa, Y., et al. 2008, Solar Phys., 249, 167
Valori, G., Green, L. M., Démoulin, P., et al. 2012, Solar Phys., 278, 73
Wang, J., Wang, H., Tang, F., Lee, J. W., & Zirin, H. 1995, Solar Phys., 160, 277
Wang, J., Zhou, G., Jin, C., & Li, H. 2012, Solar Phys., 278, 299
Yang, S., Zhang, J., & Borrero, J. M. 2009, ApJ, 703, 1012
Yang, S., Zhang, J., Li, T., & Liu, Y. 2012, ApJL, 752, L24
Zhang, J., Ma, J., & Wang, H. 2006, ApJ, 649, 464
Zhang, J., Yang, S.-H., & Jin, C.-L. 2009, RAA (Research in Astronomy and Astrophysics), 9, 921
Zhang, Q. M., Chen, P. F., Guo, Y., Fang, C., & Ding, M. D. 2012, ApJ, 746, 19
Zirin, H. 1987, Solar Phys., 110, 101